

Imaging topology of Hofstadter ribbons

Dina Genkina¹, Lauren M. Aycock^{1,2,3}, Hsin-I Lu^{1,4}, Mingwu Lu¹, Alina M. Pineiro¹, & I. B. Spielman¹

¹*Joint Quantum Institute, National Institute of Standards and Technology, and University of Maryland, Gaithersburg, Maryland, 20899, USA*

²*Department of Physics, Cornell University, Ithaca, NY 14850*

³*Currently APS/AAAS Congressional Science Fellow*

⁴*Currently Modern Electron, Bellevue, WA 98007*

Physical systems with non-trivial topological order find direct applications in metrology¹ and promise future applications in quantum computing^{2,3}. The quantum Hall effect derives from transverse conductance, quantized to unprecedented precision in accordance with the system's topology⁴. At magnetic fields beyond the reach of current condensed matter experiment, around 10^4 Tesla, this conductance remains precisely quantized but takes on different values⁵. Hitherto, quantized conductance has only been measured in extended 2-D systems. Here, we engineered and experimentally studied narrow 2-D ribbons, just 3 or 5 sites wide along one direction, using ultracold neutral atoms where such large magnetic fields can be engineered⁶⁻¹¹. We microscopically imaged the transverse spatial motion underlying the quantized Hall effect. Our measurements identify the topological Chern numbers with typical uncertainty of 5%, and show that although band topology is only properly defined in infinite systems, its signatures are striking even in nearly vanishingly thin systems.

The importance of topology in physical systems is famously evidenced by the quantum Hall effect's role as an ultra-precise realization of the von Klitzing constant $R_K = h/e^2$ of resistance¹. Although topological order is only strictly defined for infinite systems, the bulk properties of macroscopic topological systems closely resemble those of the corresponding infinite system. For 2-D systems in a magnetic field B_0 , the topology is characterized by an integer invariant called the Chern number. Even at laboratory fields of tens of Tesla, crystalline materials have a small magnetic flux $\Phi = AB_0$ per individual lattice plaquette (with area A) compared to the flux quantum $\Phi_0 = h/e$. Superlattice¹²⁻¹⁵ and ultracold atom^{7,8} systems now realize 2-D lattices in a regime where the magnetic flux per plaquette Φ is a significant fraction of Φ_0 .

Experimental signatures of Chern numbers generally leverage one of two physical effects: in condensed matter systems the edge-bulk correspondence allows the Chern number to be inferred from the quantized Hall conductivity $\sigma_H = C/R_K$, and in cold-atom experiments direct probes of the underlying band structure give access to the Chern number¹⁶⁻¹⁸. Both of these connections derive from the pioneering work of Thouless, Kohmoto, Nightingale, and den Nijs⁵, in the now famous TKNN paper. Going beyond these well known techniques, the TKNN paper showed that for rational flux $\Phi/\Phi_0 = P/Q$ (for relatively prime integers P and Q) the integer solutions s and C to the Diophantine equation

$$1 = Qs - PC \tag{1}$$

uniquely¹ determine the Chern number C . We leveraged this result to determine the Chern number

¹Subject to the constraint $|C| \leq |Q|/2^5$,¹⁹. The integer s has no physical significance as changing the flux by a multiple of 2π simply changes s by a multiple of C .

of our system.

We studied ultracold neutral atoms in a square lattice with a large magnetic flux per plaquette. As pictured in Fig. 1a, our system consisted of a 2-D lattice that is extremely narrow along one direction, just 3 or 5 sites wide - out of reach of traditional condensed matter experiments, with hard wall boundary conditions: a ribbon. Our system was well described by the Harper-Hofstadter Hamiltonian^{20,21}

$$\hat{H} = - \sum_{m,j} (|t_x| e^{i\phi m} |j, m\rangle \langle j+1, m| + t_s |j, m\rangle \langle j, m+1|) + \text{H.c.}, \quad (2)$$

where j and m label lattice sites along \mathbf{e}_x and \mathbf{e}_s , with tunneling strengths t_x and t_s respectively. As shown in Fig. 1a, tunneling along \mathbf{e}_x was accompanied by a phase shift $e^{i\phi m}$. Hopping around a single plaquette of this lattice imprints a phase ϕ , analogous to the Aharonov-Bohm phase, emulating a magnetic flux $\Phi/\Phi_0 = \phi/2\pi$. We implemented this 2-D lattice by combining a 1-D optical lattice defining sites along an extended direction \mathbf{e}_x , with atomic spin states forming lattice sites along a narrow, synthetic⁹⁻¹¹ direction \mathbf{e}_s .

This system exhibits a Hall effect, where a longitudinal force F_{\parallel} – analogous to the electric force eE_{\parallel} in electronic systems – drives a transverse ‘Hall’ current density $j_{\perp} = \sigma_H E_{\parallel}$ for non-zero Φ/Φ_0 . A longitudinal force F_x would drive a change in the dimensionless crystal momentum $\hbar\Delta q_x/\hbar G$ and a transverse displacement Δm , giving a dimensionless Hall conductivity $NG\Delta m/\Delta q_x = \sigma_H R_K = \tilde{\sigma}_H$, where G is the reciprocal lattice constant and N is the number of carriers per plaquette (see Methods). Starting with Bose-condensed atoms in the lattice’s ground state (with transverse density shown in Fig. 1a) we applied a force along \mathbf{e}_x and obtained Δm

from site resolved density distributions¹⁸ along \mathbf{e}_s (Fig. 1b). Leveraging the Diophantine equation, we further show that the force required to move the atoms a single lattice site signals the infinite system's Chern number.

Our quantum Hall ribbons were created with optically trapped ^{87}Rb Bose-Einstein condensates (BECs) in either the $F = 1$ or 2 ground state hyperfine manifold, creating 3 or 5 site-wide ribbons from the $2F + 1$ states available in either manifold. We first loaded BECs into a 1-D optical lattice along \mathbf{e}_x formed by a retro-reflected $\lambda_L = 1064$ nm laser beam. This created a lattice with period $a = \lambda_L/2$ and depth $4.4(1)E_L$, giving tunneling strength $t_x = 0.078(2)E_L$. Here, $E_L = \hbar^2 k_L^2 / 2m_{\text{Rb}}$ is the single photon recoil energy; $\hbar k_L = 2\pi\hbar/\lambda_L$ is the single photon recoil momentum; and m_{Rb} is the atomic mass. We induced tunneling along \mathbf{e}_s with strength $t_s = 6.9(4)t_x$ with either a spatially uniform rf magnetic field or two-photon Raman transitions. The rf-induced tunneling imparted no phase, giving $\phi/2\pi = 0$. In contrast the Raman coupling, formed by a pair of counter propagating laser beams with wavelength $\lambda_R = 790$ nm, imparted a phase factor of $\exp(-2ik_R x)$. Here, $\hbar k_R = 2\pi\hbar/\lambda_R$ is the Raman recoil momentum. Comparing with Eq. 2, this gives $\phi/2\pi \approx 4/3$. We then applied a force by shifting the center of the confining potential along \mathbf{e}_x , effectively applying a linear potential. Using time-of-flight (TOF) techniques¹⁰, we measured hybrid momentum/position density distributions $n(k_x, m)$, a function of momentum along \mathbf{e}_x and position along \mathbf{e}_s , as seen in Fig. 1c-d.

We measured the Hall conductivity beginning with a BEC at $q_x(t = 0) = 0$ in the lowest band with transverse position $\bar{m}_0 = 0$ (see Methods). Fig. 2a shows the band structure of our system as a function of crystal momentum along \mathbf{e}_x , with color indicating the modal position along \mathbf{e}_s .

We applied a force F_x for varying times Δt , directly changing the longitudinal crystal momentum from 0 to a final q_x and giving a transverse Hall displacement from 0 to a final \bar{m} . Figure 2b shows a collection of hybrid density distributions, where each column depicts $n(k_x, m)$ for a specific final q_x , labelled by the overall horizontal axis. For each column, the change in crystal momentum is marked by the horizontal displacement of the diffraction orders relative to their location in the central $q_x = 0$ column. The transverse displacement is visible in the overall shift in density along m as a function of q_x , i.e., between columns.

Figure 2c quantifies this Hall effect by plotting \bar{m} as a function of q_x for $\Phi/\Phi_0 = 0, -4/3$, and $4/3$. For zero flux $\Phi/\Phi_0 = 0$ (Fig. 2c top), \bar{m} was independent of q_x ; in contrast, for non-zero flux $\Phi/\Phi_0 \approx \pm 4/3$ (Fig. 2c middle, bottom), \bar{m} depends linearly on q_x with non-zero slope. These linear dependencies evoke our earlier discussion of the Hall conductance $\tilde{\sigma}_H$, in which we anticipated slopes equal to the Chern number. Linear fits to the data give $\tilde{\sigma}_H = 0.01(1), 0.87(3)$, and $-0.85(3)$ for zero, negative and positive flux respectively, showing the expected qualitative behavior. The expected slopes, given by the Chern number, $\sigma_H = 0, \pm 1$ are indicated by black dashed lines in Fig. 2c.

The red curves in Fig. 2c show the expected behavior for our 5-site wide system for adiabatic changes in q_x , always within the lowest band (Fig. 2a), i.e., Bloch oscillations. This theory predicts a nearly linear slope for small q_x sharply returning to $\bar{m} = 0$ at the edges of the Brillouin zone. A linear fit to this theory produces $\tilde{\sigma}_H \approx 0, 0.6$, and -0.6 for zero, negative and positive flux respectively, far from the Chern number. This discrepancy is resolved by recalling that Bloch oscillations require adiabatic motion, and the band gaps at the edge of the Brillouin zone close as

the ribbon width grows, making the Bloch oscillation model inapplicable. The departure of the data from the adiabatic theory at the edges of the Brillouin zone indicates a partial break down of adiabaticity was present in our data.

To better identify Chern numbers, we relate the Diophantine equation (Eqn. 1) to the physical processes present in our system. Although the Hofstadter Hamiltonian in Eqn. 2 is only invariant under m -translations that are integer multiples of Q , a so-called “magnetic-displacement” by $\Delta m = 1$ accompanied with a crystal momentum shift $\Delta q_x/2k_R = P/Q$ leaves Eqn. 2 unchanged. Together, these symmetry operations give a Q -fold reduction of the Brillouin zone along e_s , and add a Q -fold degeneracy, as illustrated in Fig. 3a for $\Phi/\Phi_0 = 0, 1/3, \text{ and } 2/5$. Recalling that the Brillouin zone is $2\hbar k_L$ periodic along e_x , it follows that a displacement by $2k_L/Q$ to the nearest symmetry related state involves an integer C magnetic displacements, shown in Fig. 3b for $\Phi/\Phi_0 = 1/3$ and $2/5$, given by solutions to $2k_L s - 2k_R C = 2k_L/Q$, where s counts the number of times the Brillouin zone was “wrapped around” during the C vertical displacements. Because this is no more than a re-expression of the Diophantine equation, we identify C as the Chern number. Both C and s directly relate to physical processes. First, each time the Brillouin zone is wrapped around implying a net change of momentum by $2\hbar k_L$ a pair of photons must be exchanged between the optical lattice laser beams. Second, each change of m by 1 must be accompanied by a $2\hbar k_R$ recoil kick imparted by the Raman lasers as they change the spin state. This physical motivation of the Diophantine equation remains broadly applicable even for our narrow lattice, providing an alternate signature of the Chern number.

Figure 4 shows the full evolution of fractional population in each m site as a function of crys-

tal momentum q_x in the lowest band. The black circles locate the peak of the fractional population in each spin state. We identify the crystal momenta at which the wavefunction was displaced by a single lattice site along \mathbf{e}_s starting at $q_x = 0$, similar to the suggestions in Refs. ^{22,23}. We associate the Chern number with the slope of a linear fit through the three peak locations. For the 3-site wide ribbon, we measured a Chern number of 0.99(4), $-0.98(5)$ for negative and positive flux respectively², in agreement with the exact theory, which predicts $\pm 0.97(1)$. For the 5-site wide ribbon, we measured 1.11(2), $-0.97(4)$, close to the theoretical prediction of $\pm 1.07(1)$. The deviation from unity results from $\Phi/\Phi_0 - 4/3 \approx 0.01$, a non-zero quadratic Zeeman shift, and $t_s > t_x$ allowing hybridization of the edge states²³.

Our direct microscopic observations of topologically driven transverse transport demonstrate the power of combining momentum and site-resolved position measurements. With interactions, these systems are predicted to give rise to complex phase diagrams supporting vortex lattices and charge density waves^{24–26}. Realizations of controlled cyclic coupling giving periodic boundary conditions⁹ along \mathbf{e}_s could elucidate the appearance of edge modes as the coupling between two of the three states is smoothly tuned to zero. In addition, due to the non-trivial topology as well as the low heating afforded by synthetic dimensional systems, a quantum Fermi gas dressed similarly to our system would be a good candidate for realizing fractional Chern insulators²⁷.

²Our Chern number extraction scheme fails for the rf case as the fractional populations are flat and there is no peak. We therefore assign a Chern number of 0 to flat distributions.

Methods

Experiment We created nearly pure ^{87}Rb BECs in a crossed optical dipole trap¹⁰ with frequencies $(\omega_x, \omega_y, \omega_z)/2\pi = (27.1(2), 58.4(8), 94.2(5))$ Hz. We deliberately used small, low density BECs with $\approx 10^3$ atoms to limit unwanted scattering processes in regimes of dynamical instability²⁸. At various times in the sequence, we used coherent rf and microwave techniques to prepare the hyperfine $|F, m_F\rangle$ state of interest. The 1-D optical lattice was always ramped on linearly in 300 ms. For non-zero ϕ , we turned on the Raman beams adiabatically in 30 ms after ramping on the lattice. For $\phi = 0$ we used adiabatic rapid passage starting in $m_F = -F$ and swept the bias magnetic field in ≈ 50 ms to resonance. We applied forces by spatially displacing the optical dipole beam providing longitudinal confinement (by frequency shifting an acousto-optic modulator), effectively adding a linear contribution to the existent harmonic potential for displacements small compared to the beam waist.

We define the modal position \bar{m} as the center of a Gaussian fit to the population distribution along \mathbf{e}_s .

Rf correction. In experiments where the tunneling along \mathbf{e}_s was induced by a uniform rf magnetic field ($\Phi/\Phi_0 = 0$), our loading procedure had remnant non-adiabaticity that led to temporal oscillations in the fractional populations in different m states at the 40% level. To separate the effects due to this non-adiabaticity from transverse transport, we performed the experiment with identical preparations without applying the longitudinal force. We then used the observed oscillations as a function of time without an applied force as a baseline, and report the difference in fractional

populations between that baseline and the cases where the force was applied.

Hall conductivity The current density can be expressed as $j_{\perp} = n_{2D}v_{\perp}e$, where n_{2D} is the 2-D charge carrier density, v_{\perp} is the transverse velocity and e is the electron charge. Using $\sigma_H E_{\parallel} = F_{\parallel}\sigma_H/e$, and choosing some increment of time Δt , we have $v_{\perp} = \Delta x_{\perp}/\Delta t$, and $F_{\parallel} = \hbar\Delta q_{\parallel}/\Delta t$, where q_{\parallel} is the crystal momentum along the direction of the force. Re-expressing n_{2D} in number of carriers N per plaquette, defining Δx_{\perp} as transverse displacement in units of lattice periods, we obtain $NG\Delta x_{\perp}/\Delta q_{\parallel} = \sigma_H R_K$.

1. Klitzing, K. v., Dorda, G. & Pepper, M. New method for high-accuracy determination of the fine-structure constant based on quantized hall resistance. *Phys. Rev. Lett.* **45**, 494–497 (1980).
2. Freedman, M. H. Quantum computation and the localization of modular functors. *Foundations of Computational Mathematics* **1**, 183–204 (2001).
3. Kitaev, A. Fault-tolerant quantum computation by anyons. *Annals of Physics* **303**, 2 – 30 (2003).
4. Laughlin, R. B. Quantized hall conductivity in two dimensions. *Phys. Rev. B* **23**, 5632–5633 (1981).
5. Thouless, D. J., Kohmoto, M., Nightingale, M. P. & den Nijs, M. Quantized hall conductance in a two-dimensional periodic potential. *Phys. Rev. Lett.* **49**, 405–408 (1982).
6. D. Jaksch, P. Z. Creation of effective magnetic fields in optical lattices: the hofstadter butterfly for cold neutral atoms. *New Journal of Physics* **5**, 56 (2003).

7. Miyake, H., Siviloglou, G. A., Kennedy, C. J., Burton, W. C. & Ketterle, W. Realizing the harper hamiltonian with laser-assisted tunneling in optical lattices. *Phys. Rev. Lett.* **111**, 185302 (2013).
8. Aidelsburger, M. *et al.* Realization of the hofstadter hamiltonian with ultracold atoms in optical lattices. *Phys. Rev. Lett.* **111**, 185301– (2013).
9. Celi, A. *et al.* Synthetic gauge fields in synthetic dimensions. *Phys. Rev. Lett.* **112**, 043001– (2014).
10. Stuhl, B. K., Lu, H.-I., Ayccock, L. M., Genkina, D. & Spielman, I. B. Visualizing edge states with an atomic bose gas in the quantum hall regime. *Science* **349**, 1514– (2015).
11. Mancini, M. *et al.* Observation of chiral edge states with neutral fermions in synthetic hall ribbons. *Science* **349**, 1510– (2015).
12. Geisler, M. C. *et al.* Detection of a landau band-coupling-induced rearrangement of the hofstadter butterfly. *Phys. Rev. Lett.* **92**, 256801 (2004).
13. Melinte, S. *et al.* Laterally modulated 2d electron system in the extreme quantum limit. *Phys. Rev. Lett.* **92**, 036802 (2004).
14. Feil, T., Výborný, K., Smrčka, L., Gerl, C. & Wegscheider, W. Vanishing cyclotron gaps in a two-dimensional electron system with a strong short-period modulation. *Phys. Rev. B* **75**, 075303 (2007). URL <https://link.aps.org/doi/10.1103/PhysRevB.75.075303>.

15. Dean, C. R. *et al.* Hofstadter’s butterfly and the fractal quantum hall effect in moiré superlattices. *Nature* **497**, 598– (2013).
16. Jotzu, G. *et al.* Experimental realization of the topological haldane model with ultracold fermions. *Nature* **515**, 237–240 (2014).
17. Aidelsburger, M. *et al.* Measuring the chern number of hofstadter bands with ultracold bosonic atoms. *Nat Phys* **11**, 162–166 (2015).
18. Wang, L., Soluyanov, A. A. & Troyer, M. Proposal for direct measurement of topological invariants in optical lattices. *Phys. Rev. Lett.* **110**, 166802– (2013).
19. Kohmoto, M. Zero modes and the quantized hall conductance of the two-dimensional lattice in a magnetic field. *Phys. Rev. B* **39**, 11943–11949 (1989).
20. Harper, P. G. Single band motion of conduction electrons in a uniform magnetic field. *Proceedings of the Physical Society. Section A* **68**, 874 (1955).
21. Hofstadter, D. R. Energy levels and wave functions of bloch electrons in rational and irrational magnetic fields. *Phys. Rev. B* **14**, 2239–2249 (1976).
22. Zhang, D.-W. & Cao, S. Measuring the spin chern number in time-reversal-invariant hofstadter optical lattices. *Physics Letters A* **380**, 3541–3545 (2016).
23. Muga, S. *et al.* Measuring chern numbers in hofstadter strips. *SciPost* (2017).
24. Greschner, S. *et al.* Spontaneous increase of magnetic flux and chiral-current reversal in bosonic ladders: Swimming against the tide. *Phys. Rev. Lett.* **115**, 190402 (2015).

25. Greschner, S. *et al.* Symmetry-broken states in a system of interacting bosons on a two-leg ladder with a uniform abelian gauge field. *Phys. Rev. A* **94**, 063628 (2016).
26. Calvanese Strinati, M. *et al.* Laughlin-like states in bosonic and fermionic atomic synthetic ladders. *Phys. Rev. X* **7**, 021033 (2017).
27. Parameswaran, S. A., Roy, R. & Sondhi, S. L. Fractional quantum hall physics in topological flat bands. *Comptes Rendus Physique* **14**, 816–839 (2013).
28. Campbell, G. K. *et al.* Parametric amplification of scattered atom pairs. *Phys. Rev. Lett.* **96**, 020406 (2006).

Acknowledgments This work was partially supported by the Air Force Office of Scientific Research’s Quantum Matter MURI, NIST, and NSF (through the Physics Frontier Center at the JQI).

Author Contributions D.G. configured the apparatus for this experiment and led the team on all aspects of the measurements. All authors except I.B.S contributed to the data collection effort. D.G. performed calculations and analyzed data. All authors contributed to writing the manuscript. I.B.S. proposed the experiment concept and wrote this statement.

Competing Interests The authors declare that they have no competing financial interests.

Correspondence Correspondence and requests for materials should be addressed to I.B.S. (email: ian.spielman@nist.gov).

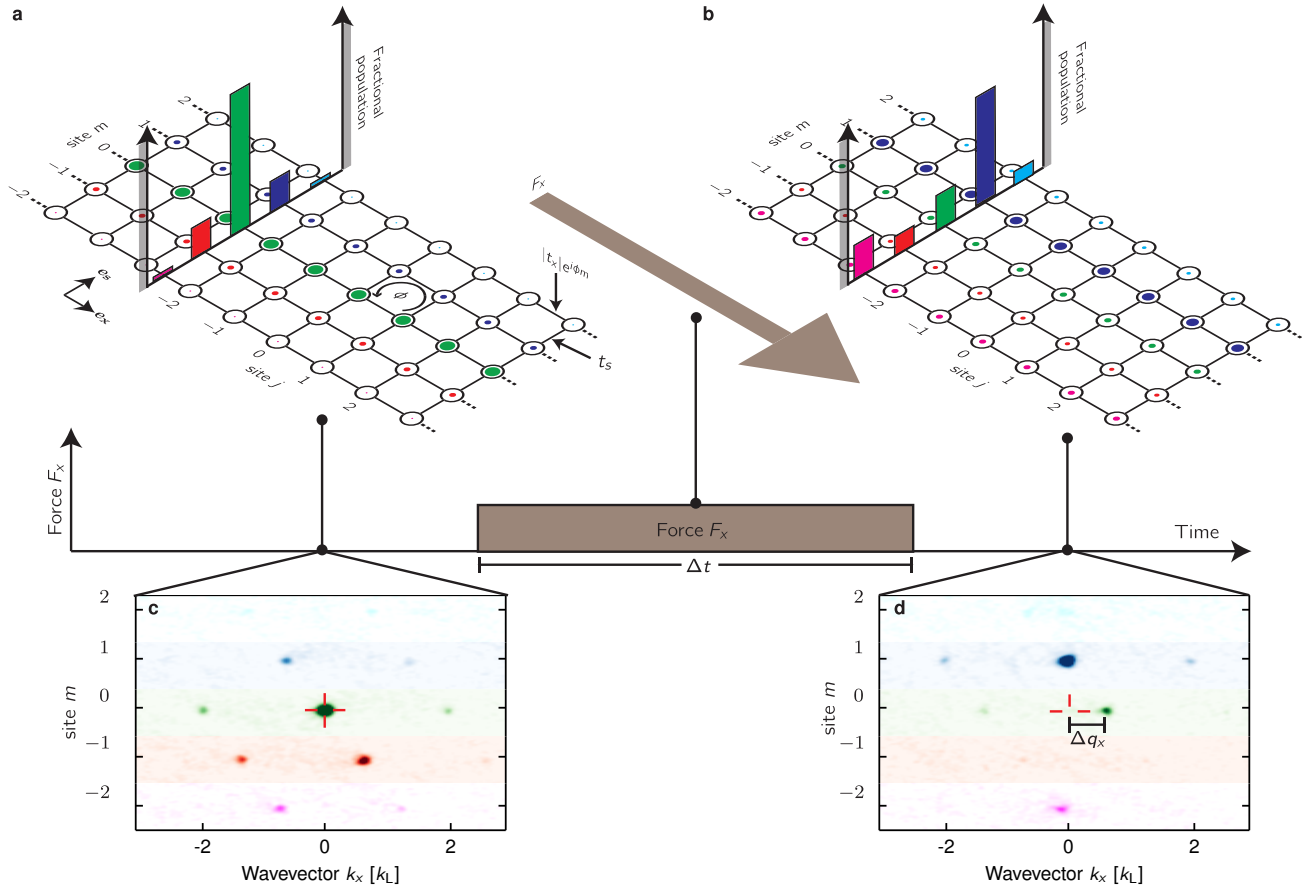


Figure 1 | Quantum Hall effect in Hofstadter ribbons. **a.** 5-site wide ribbon with real tunneling coefficients along \mathbf{e}_s and complex tunneling coefficients along \mathbf{e}_x , creating a non-zero phase ϕ around each plaquette. **b.** After applying a force along \mathbf{e}_x for a time Δt , atomic populations shift transversely along \mathbf{e}_s , signaling the Hall effect. **c,d.** TOF absorption images giving hybrid momentum/position density distributions $n(k_x, m)$. Prior to applying the force **c**, the $m = 0$ momentum peak is at $k_x = 0$, marked by the red cross. Then, in **d**, the force directly changed q_x , evidenced by the displacement Δq_x of crystal momentum, and via the Hall effect shifted population along \mathbf{e}_s .

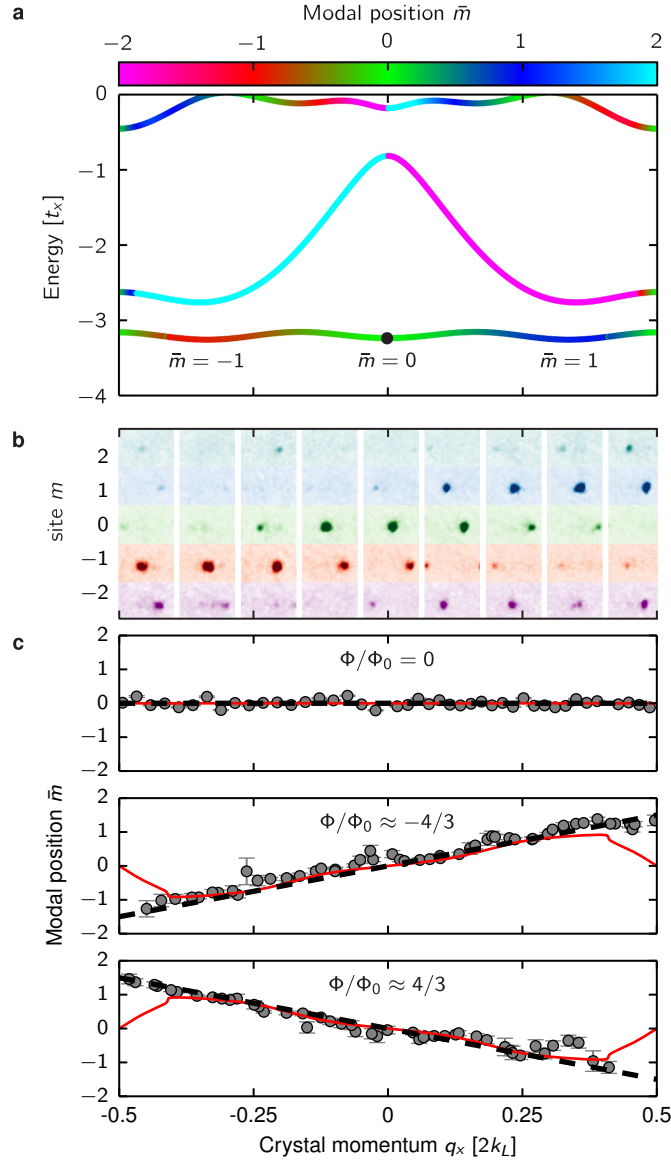


Figure 2 | Hall displacement in a 5-site wide ribbon. **a.** Band structure computed for a $4.4E_L$ deep 1-D lattice ($\lambda_L = 1064$ nm), $0.5E_L$ Raman coupling strength ($\lambda_R = 790$ nm), and quadratic Zeeman shift $\epsilon = 0.02E_L$, giving $\Phi/\Phi_0 \approx 4/3$, $t_x = 0.078E_L$, $t_s = 6.4t_x$. The color indicates modal position \bar{m} . The black dot indicates the initial loading parameters. **b.** TOF absorption images $n(k_x, m)$ for varying longitudinal crystal momenta q_x . **c.** Transverse displacement. Modal position \bar{m} is plotted as a function of q_x for $\Phi/\Phi_0 \approx 0, -4/3, 4/3$ (top, middle, and bottom respectively). Gray circles depict the measurements; black dashed lines are the prediction of our simple $\tilde{\sigma}_H$ and red curves are the expectation from the band structure of our thin ribbon. As discussed in the methods, the $\Phi/\Phi_0 = 0$ data was compensated to account for non-adiabaticity in the loading procedure.

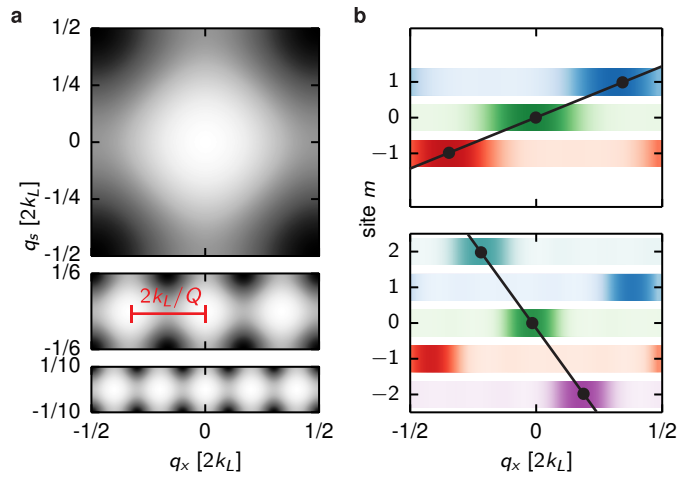


Figure 3 | Chern number from the Diophantine equation. **a.** Lowest band energy within the Brillouin zone in an extended 2-D system, where q_x and q_s are crystal momenta along \mathbf{e}_x and \mathbf{e}_s , respectively. Top. $\Phi/\Phi_0 = 0$. Middle. $\Phi/\Phi_0 = 1/3$: Brillouin zone shrinks by a factor of 3 and becomes 3-fold degenerate, distance between adjacent energy minima spaced by $2k_L/Q$ is labeled. Bottom. $\Phi/\Phi_0 = 2/5$. **b.** Fractional population in each spin state in the lowest band at $q_s = 0$. Top. $\Phi/\Phi_0 = 1/3$. Bottom. $\Phi/\Phi_0 = 2/5$. A momentum shift along \mathbf{e}_x of $2k_L/Q$ is accompanied by an integer number of spin flips C . A line connecting magnetic states separated by $2k_L/Q$, with slope $C = 1$ (top) and -2 (bottom), is indicated.

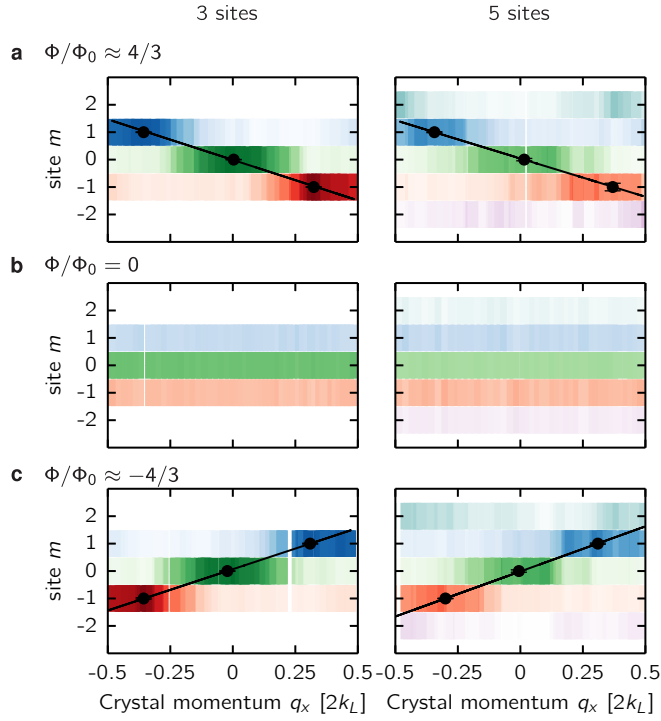


Figure 4 | Chern number measurement. Lowest band fractional population measured as a function of crystal momentum in the \mathbf{e}_x and position in the \mathbf{e}_s . Darker color indicates higher fractional population. In the Raman-coupled cases, the points represent the fitted population maxima and the Chern number is extracted from the best fit line to those points. **a.** 3-site (left) and 5-site (right) systems with positive flux. **b** 3-site (left) and 5-site (right) system with zero flux. **c.** 3-site (left) and 5-site (right) systems with negative flux.